Supporting Information

Disentangling the Activity-Charge Coupling in Cocatalyst–Semiconductor Heterojunctions for Optimized Oxygen Evolution

Ying Liu,[1§] Min Zhou,[1§] Guanhua Ren,[1] Peijun Hu[1,2,3] and Haifeng Wang[1*]

[1]State Key Laboratory of Green Chemical Engineering and Industrial Catalysis, Centre for Computational Chemistry and Research Institute of Industrial Catalysis, East China University of Science and Technology, Shanghai 200237, China

[2]School of Chemistry and Chemical Engineering, The Queen's University of Belfast, Belfast BT9 5AG, U.K.

[3]School of Physical Science and Technology, ShanghaiTech University, Shanghai 201210, China

*Corresponding author: hfwang@ecust.edu.cn

Section 1: Water/TiO_2 interface models and Ab initio molecular dynamics simulation

To model the aqueous environment at the IrO_2/TiO_2 interface, we performed *ab-initio* molecular dynamics (AIMD) simulations. A total of 26 randomly connected H_2O molecules, confined by Ar atoms above the slab, were introduced to form the initial aqueous network. The number of liquid water molecules was adjusted to achieve the experimental density of water (1.0 g/cm^3), based on fixed lateral lattice constants along the *a* and *b* directions (Figure S3a). AIMD simulations were carried out over a period of 10 ps, with equilibrium reached in cases after approximately 5 ps (see Figure S3b). Interface structures for subsequent calculations were sampled from the later stage of the AIMD trajectory, after equilibrium had been established. To calculate the reaction energies at the liquid/solid interface, the multipoint averaging molecular dynamics (MPA-MD) method was applied for each intermediate state (IMS, including transition states) at the aqueous IrO_2/TiO_2 interface. This approach, established in our previous study, has been shown to provide accurate evaluations of solvation energy.[1] First, ~10 snapshots were selected every 0.2 ps from the equilibrated trajectory and further optimized to obtain the total energy of each structure (E_{tot}) using the PBE+U method. Second, to account for the variations in the surrounding water networks on E_{tot}, the total energy of the water structure (E_{water}) was subtracted, yielding the 'solvation-included energy' ($E_{sol\text{-}included}$). This quantity incorporates the solvation effect for each configuration, while the fluctuation remains relatively small because the intrinsic flexibility of the water structure has been removed. Detailed definition of 'solvation-included energy' and the 'averaging' protocol are provided below.

For an IMS *i* in photocatalytic OER, we selected and optimized *j* samples from AIMD simulations, and the total energy of each sample can be expressed as:

$$E_{\mathrm{tot}}^{\mathrm{i,j}} = E_{\mathrm{water}}^{\mathrm{i,j}} + E_{\mathrm{catal}}^{\mathrm{i,j}} + E_{\mathrm{int}}^{\mathrm{i,j}} \quad \text{(S1)}$$

where $E_{water}^{i,j}$, $E_{catal}^{i,j}$, and $E_{int}^{i,j}$ are the computed energies of water solution, catalyst surface (including the reaction center) and the interactions between the water solution and catalyst surface, respectively.

For reactions without the water molecules, $E_{tot}^{i,j} = E_{catal}^{i,j}$ and thus the reaction energy can be directly computed:

$$\Delta E_{\mathrm{gas}} = \frac{1}{\mathrm{j}}\sum_{1}^{\mathrm{j}} E_{\mathrm{tot}}^{\mathrm{i+1}} - \frac{1}{\mathrm{j}}\sum_{1}^{\mathrm{j}} E_{\mathrm{tot}}^{\mathrm{i}} \quad \text{(S2)}$$

However, for reactions at the liquid/solid interface, different solution configuration of water network $E_{water}^{i,j}$ affects $E_{tot}^{i,j}$. Thus, we proposed to deduct the contribution of $E_{water}^{i,j}$ from $E_{tot}^{i,j}$ but to keep the solvation effect into consideration. Accordingly, the solvation-included energy is defined as:

$$E_{\mathrm{sol\text{-}included}}^{\mathrm{i,j}} = E_{\mathrm{catal}}^{\mathrm{i,j}} + E_{\mathrm{int}}^{\mathrm{i,j}} = E_{\mathrm{tot}}^{\mathrm{i,j}} - E_{\mathrm{water}}^{\mathrm{i,j}} \quad \text{(S3)}$$

and the reaction energy can be computed using the 'averaging' approach:

$$\Delta E_{\text{interface}} = \frac{1}{\text{j}}\sum_{1}^{\text{j}} E_{\text{sol - included}}^{\text{i+1}} - \frac{1}{\text{j}}\sum_{1}^{\text{j}} E_{\text{sol - included}}^{\text{i}} \quad \text{(S4)}$$

which not only contains the reaction energy without the water molecules, but also includes the solvation effect of the water environment.

The adsorption energy of X species (E_{ads}(X)) is defined as follows:

$$E_{\text{ads}}(\text{X}) = E_{total} - E_{surface} - E_X \quad \text{(S5)}$$

where E_{surface}, E_{X} and E_{total} are the energies for the clean surface, X species phase and X species adsorbed on the surface in the aqueous solution, respectively. The more negative the E_{ads}(X) is, the stronger species X binds on the surface. The entropy effect was included in calculating the adsorption of H_2O and desorption of O_2.

The binding energy (E_{b}) of IrO_2 layers on TiO_2(110) is defined as follows:

$$E_{\text{b}} = (E_{IrO_2/TiO_2} - E_{IrO_2} - E_{TiO_2})/S \quad \text{(S6)}$$

where E_{IrO_2/TiO_2}, E_{IrO_2} and E_{TiO_2} are the energies of IrO_2/TiO_2 interface, IrO_2 layers and TiO_2 single crystal supercell, respectively. *S* represents the interfaces area.

Section 2: Details of the microkinetic modeling

To quantitatively evaluate the photocatalytic OER performance, the CATKINAS package was used[2], a widely used microkinetic simulation tool developed by our group.[1, 3-6] The reaction kinetics were solved under the steady-state condition, without assuming a particular step to be slowest or rate-limiting one, within the framework of transition state theory.

For each elementary step *i,* according to the De Donder relation,[7] the reaction rate can be written as:

$$\begin{aligned} R_{\text{i}} &= r_{i+} - r_{i-} = k_{i+}\text{C}_{1+}\text{C}_{2+}\cdots\theta_{1+}\theta_{2+}\cdots - k_{i-}\text{C}_{1-}\text{C}_{2-}\cdots\theta_{1-}\theta_{2-}\cdots \\ &= k_{i+}\text{C}_{1+}\text{C}_{2+}\cdots\theta_{1+}\theta_{2+}\cdots(1 - Z_i) \end{aligned} \quad \text{(S7)}$$

where k_{i+} is the forward rate constant of step *i*; $k_{\text{i}-}$ is the reverse rate constant of step *i*; θ is the coverage of surface species *j* or surface free site *; C is the concentration of an individual reactant or product; $Z_i = \frac{Q_i}{K_{i,eq}}$ is reaction reversibility of step *i*, which approaches zero as step *i* becomes irreversible and reaches unity as step *i* becomes quasi-equilibrated; $Q_i = \frac{C_{1-}C_{2-}\theta_{1-}\theta_{2-}}{C_{1+}C_{2+}\theta_{1+}\theta_{2+}}$ and $K_{i,\,eq} = \exp\left(-\frac{\Delta G_i^{\ominus}}{RT}\right)$ are the reaction quotient and the equilibrium constant of step *i*, respectively. k_{i+} is determined from the transition state theory, which can be written as:

$$k_{i+} = \frac{k_B T}{h} \exp\left(\frac{\Delta S_i}{R}\right) \exp\left(-\frac{E_{a,i}}{RT}\right) \quad \text{(S8)}$$

where k_B and h are Boltzmann constants and T is the reaction temperature.

At the steady-state condition, the coverage θ of free sites and all intermediates j follows the conservation rule:

$$\sum_j \varphi_j = 1 \quad \text{(S9)}$$

The rate of change of all the coverage is zero, that is:

$$\frac{\partial \varphi_j}{\partial t} = 0 \quad \text{(S10)}$$

Based on the reaction barrier (E_a) and free energy change (ΔG) of each elementary reaction step i (Table S6), microkinetic analysis of photocatalytic OER over $IrO_2/TiO_2(110)$ was performed under the condition of $X_{H_2O(aq)}$= 1 (mole fraction), $X_{O_2(aq)}$= 10^{-7}, pH = 7 (Notably, in the present work, we considered that practical photocatalytic reactions typically occur under near-neutral conditions, and therefore set pH = 7. It should be noted, however, that the activity and stability of photocatalysts can depend on the solution pH. In future studies, the influence of pH on catalytic activity and stability could be explored using two possible approaches: (i) adjusting the proton concentration in the kinetic model and correcting the reaction free energies accordingly, which offers a computationally efficient approximation; or (ii) explicitly including H^+ ions in the simulation, if sufficient computational resources are available, allowing a more accurate atomic-scale investigation of pH effects on reaction kinetics.) and T = 300 K. The hole diffusion barrier was set to ~0.25 eV[8] with the surface-reaching hole concentration (C_{h+}) of 10^{-9} ML on the $TiO_2(110)$ surface[9], consistent with our previous work[1]. On the IrO_2/TiO_2 surface, this value is estimated to be ~10^4 times higher than that at O_{2c}^{2-} at room temperature, as determined using the Boltzmann distribution function, $p_1/p_2 = exp[(0.66–0.42)\ eV/(k_B T)]$, where p_1 and p_2 represent the populations of h^+ trapped by the IrO_2 layer and O_{2c}^{2-}, respectively. Accordingly, C_{h+} on IrO_2/TiO_2 is approximately 10^{-5} ML, compared to 10^{-9} ML on TiO_2. To systematically assess the effect of C_{h+}, we varied its value from 10^{-9} (very low) to 10^0 (very high) ML in our kinetic simulations (Figure 4, main text). Notably, these calculations effectively represent a sensitivity analysis with respect to HAC as a variation in HAC (e.g., ±0.1 eV in hole stabilization energy) directly translates into a change in the equilibrium surface hole concentration C_{h^+}. The rate constant (k) of each step was calculated using the transition state theory, while collision theory was applied to describe the adsorption/desorption process. The reaction rate (r_i), the reversibility (Z_i) and the degree of rate control (DRC) of each step i are presented in Table S8.

In our work, DRC calculations follow the definition by Campbell et al.[11, 12]. Specifically, Campbell introduced the degree of rate control $X_{RC,i}$ for an elementary step i, which is denfined as:

$$X_{RC,i} = \frac{k_i}{r}\left(\frac{\partial r}{\partial k_i}\right)_{k_{j\neq i}, K_i} = \left(\frac{\partial \ln r}{\partial \ln k_i}\right)_{k_{j\neq i}, K_i} \quad \text{(S11)}$$

where the partial derivative is taken holding constant the rate constants, k_j, for all other steps $j \neq i$ and the equilibrium constant, K_i, for step i (and all other steps too, since their forward and reverse rate constants are held fixed). Keeping K_i constant means that k_i and k_{-i} be varied by equal factors so that their ratio remains unchanged. Within transition-state theory, this is implemented by changing only the free energy of the transition state for step i without altering the standard-state free energies of other transition states, reactants, products, or intermediates, as the rate constant $k_i = (k_B T/h) \exp(-\Delta G^{0,TS}_i/RT)$, where ΔG_{0i}^{TS} is the standard-state molar free energy difference between the transition state and the reactants, k_B is Boltzmann's constant, and h is Planck's constant. The equilibrium constant $K_i = \exp(-\Delta G^{0,rxn}_i/RT)$, where $\Delta G^{0,rxn}_i$ is the standard-state free energy difference between products and reactants.

Moreover, we investigated the influence of different kinetic barriers of O-O bond formation via the I2M/WNA and of C_{h+} on the total turnover frequency (TOF, which is a quantitative measure of the overall rate), using an approach similar to that proposed in ref. *10* (that is, degree of rate control). Specifically, the barriers of other steps were kept constant, while the TOF values were mapped by solving the kinetic equations at every single point. The I2M and WNA barrier were varied along the x-axis from 0 to 6.0 eV and from 0 to 1.6 eV, respectively, at intervals of 0.2, while $\log_{10}C_{h+}$ was varied along the y-axis from -12 to 0 at intervals of 1 (Figure S19).

For the surface reactions, the free energy of elementary reaction can be calculated with $\Delta G = \Delta H - T\Delta S + \Delta E_{ZPE}$, ΔH is the enthalpy change, and $T\Delta S$ is the entropy change and can be obtained from the Handbook of Chemistry and Physics[13]. E_{ZPE} is the zero-point energy, which can be obtained through vibrational Frequency calculations. For surface reactions with no adsorption/desorption processes, the values of $T\Delta S$ are typically small, and can thereby be neglected[14]. The free energy changes of surface reactions can be approximately estimated from the enthalpy change. However, for the H_2O adsorption (step 1) and O_2 desorption (step 11) processes, the entropy and zero-point energy corrections should be considered and have displayed in Table S9.

Section 3: Simulation of hole trapping in the system

To avoid potentially misleading energy results from background charge corrections, we simulated trapped h^+ or surface radicals by introducing an OH group on the opposite surface instead of extracting electrons from the system. By introducing an OH group as an electron acceptor on the bottom surface, an electron is trapped at the OH group, forming surface OH^- and enabling the simulation of a h^+ within a charge-neutral system (Figure S6). The localization of the h^+ was further confirmed by the electronic structure analysis, including site-projected magnetic moment and Bader charge analysis. Similar approaches have been employed in our previous

work.[1, 14-18]

The stability of holes localized in different regions of the system is quantified by the hole accumulation capacity (HAC). The HAC value is calculated as the energy difference between an h^+ localized at a specific site and the reference state in which the h^+ resides on a bulk lattice oxygen ($O_{bulk}^{\bullet-}$). Taking $^*O_{2c}^{2-} + O_{bulk}^{\bullet-} + {}^*OH^-_{bottom} \rightarrow {}^*O_{2c}^{\bullet-} + O_{bulk}^{2-} + {}^*OH^-_{bottom}$ as an example (Figure S6), the HAC of O_{2c}^{2-} site is defined as the reaction energy obtained by comparing the total energy of two systems: (i) an h^+ localized on $O_{bulk}^{\bullet-}$(reference state), and (ii) an h^+ localized at the surface lattice oxygen ($O_{2c}^{\bullet-}$).

For reaction mechanism calculations on IrO_2/TiO_2, the treatment of the first and second h^+ introduction depends on the specific elementary step (Figure S7): (i) For the initial H_2O deprotonation step ($^*H_2O \rightarrow {}^*OH^- + {}^*H^+$), h^+ does not participate directly in the reaction. In this case, an OH^-_{bottom} can be introduced, with the accompanying h^+ trapped in the TiO_2 bulk. Alternatively, this OH^-_{bottom}/h^+ pair can be omitted without affecting the reaction mechanism. (ii) In the second elementary step, OH^- captures one h^+ and deprotonates to form an $O^{\bullet-}$ radical and H^+. This process can be modeled in two ways: (a) $^*OH^- + {}^*H^+ + h^+ + {}^*OH^-_{bottom} \rightarrow {}^*OH^{\bullet} + {}^*H^+ + {}^*OH^-_{bottom} \rightarrow O^{\bullet-} + 2H^+ + {}^*OH^-_{bottom}$), where one OH^-_{bottom} is present used to introduce an h^+; or (b) $^*OH^- + h^+ \rightarrow {}^*OH^{\bullet} \rightarrow {}^*O^{\bullet-} + {}^*H^+$, where the OH^-_{bottom} and the H^+ generated in step (ii) are simultaneously removed, and in this case OH^-_{bottom} is not explicitly included. The energetics of these two treatments are comparable due to the relatively weak electrostatic interactions. (iii) The third step involves O-O bond formation through the WNA mechanism, in which two h^+ are required and a second OH^-_{bottom} can be introduced to form a dual-hole center: $^*O^{\bullet-} + H_2O + 2{}^*H^+ + h^+ + 2{}^*OH^-_{bottom} \rightarrow {}^*OOH^- + 3{}^*H^+ + 2{}^*OH^-_{bottom}$. However, introducing multiple OH^-_{bottom} species in a finite-size catalyst model may lead to artificial structural distortions and added complexity. Thus, we alternatively simulate this process by removing two OH^-_{bottom}/H^+ pairs from both sides of the reaction, representing the reaction as $^*O^{\bullet-} + h^+ + H_2O \rightarrow {}^*OOH^- + {}^*H^+$. This simplified scheme maintains charge neutrality and achieves the correct h^+ stoichiometry while minimizing model interference. Correspondingly, the OER network is constructed within a canonical, charge-neutral photocatalytic framework.

Notably, in this strategy, the uncertain and relatively small electron–hole interaction associated with different trapping centers in the TiO_2 lattice is intentionally neglected. This simplification allows us to introduce a single localized hole without explicitly modeling the accompanying photoexcited electron. In addition, the use of an OH group on the bottom surface leads to a slightly asymmetric slab, which stabilizes the trapped hole while maintaining overall charge neutrality in the periodic system and avoids the artificial energy corrections that would otherwise arise from a compensating background charge. Although these approximations limit the explicit description of

the full electron–hole pair, they represent a widely adopted and practical approach for isolating and analyzing the structural and electronic response of a localized hole on oxide surfaces.

Section 4: Hole trapping under aqueous conditions

To examine the effect of water solution on h^+ trapping, we simulated the h^+ localization under explicit water environment. The results indicate that the h^+ remains within IrO_2, with its charge totally reduced by +0.97 |e|. Although the presence of explicit water solution has a negligible effect on the overall charge change, the distribution of h^+ in IrO_2 varies. Under gas-phase conditions, the spin density increases notably in the second IrO_2 layer, indicating preferential h^+ trapping in subsurface sites. In contrast, under water solution, the surface Ir atoms are coordinated by adsorbed H_2O molecules, effectively mimicking bulk-like coordination. This stabilizes the surface Ir atoms and results in a more uniform h^+ distribution, with enhanced spin density on the surface compared to the subsurface layer (Figure S8a, S8b). Thus, while the total localization remains within IrO_2, the presence of water solution shifts h^+ closer to the surface.

In addition, we note that no spin density is observed on the water molecules in solution, indicating that solution-water does not trap h^+. This can be attributed to the fact that the HOMO energy level of O in H_2O is significantly lower than the VBM (2.32 eV) of IrO_2/TiO_2 according to the projected density of states (PDOS) (Figure S8c). This point that water cannot localize h^+ aligns with findings from other literature studies.[19-22] Although water itself cannot localize h^+, it affects the catalyst's electronic structure. With h^+ distributed on the catalyst surface, the average distance between the H_2O and Ir site is reduced by 0.003 Å compared to the case without h^+, resulting in strengthened adsorption. This enhancement arises from a coordination interaction: the oxidized Ir center (Ir^{n+}, with higher oxidation state due to h^+ localization) provides empty d-orbitals that accept electron donation from the lone pairs on H_2O, thus strengthening the bonding interaction.

Section 5: The O-O bond formation and hole accumulation on rutile-type MO_2(110)

We evaluated the intrinsic catalytic activity for O-O bond formation by loading other rutile-type metal oxides (MnO_2, CrO_2, RhO_2, RuO_2, OsO_2 and WO_2) on TiO_2, using structures analogues to IrO_2/TiO_2 (Figure S16). Table S10 summarizes the O-O bond formation barriers via the I2M or WNA on these surfaces, along with other relevant parameters. Our primary focus is to explore activity trends across different cocatalysts. Considering computational complexity and cost, we adopt a first-order approximation by neglecting coverage and solvation effects when calculating energy barriers. The results indicate that the energy barrier decreases linearly with increasing $E_{ads}(O@M_{5c})$, consistent with the expectation that O-O bond formation becomes easier as O-M_{5c} bond weakens (Figure S17). The I2M and WNA barriers exhibit strong correlations with $E_{ads}(O@M_{5c})$, with R^2 = 0.93 and 0.90, respectively. The energies of the other reaction steps are provided in Table S11.

For the photocatalytic reaction, it should be noted that loading different cocatalysts also affects the HAC. As shown in Table S10, the HAC value indicates that h^+ preferentially localizes in the MO_2 layer. It is worth noting that, although h^+ localization and subsequent transfer to MO_2, might slightly reduce the oxidizing power of h^+, the h^+ remain capable of oxidizing water to oxygen, as shown in Figure S18. To estimate the C_{h+} on the MO_2/TiO_2 surface, the Boltzmann distribution function can be applied, $p_1/p_2=exp[\Delta HAC/(k_BT)$, where p_1 and p_2 represent the populations of h^+ trapped by the MO_2 layer and O_{2c}^{2-} sites, respectively. From this, the possibility of h^+ localization on MO_2 at the experimental temperature (300 K) with $C_{h+} = (p_1/p_2)\times10^{-9}$ ML. The calculated C_{h+} on other surfaces are shown in Table S12.

Figures and Tables

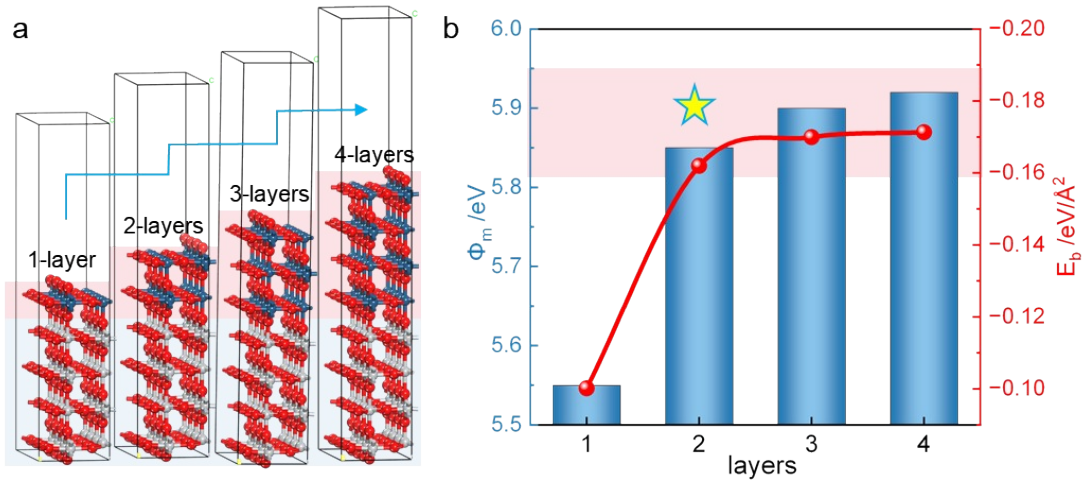

Figure S1. (a) The structures of IrO_2/TiO_2 heterojunction with one-, two-, three- and four layers IrO_2. (b) The work function (ϕ_m) and E_b change as IrO_2 layers increasing.

Note: As shown in Figure S1b, for the different layers of IrO_2, the ϕ_m is similar for 2~4 layers, and is notably higher than that of a single layer. This difference, in turn, affects the reactivity. Additionally, as the number of IrO_2 layers increases, the heterojunction binding energy (E_b) becomes more negative, indicating enhanced structure stability. Specifically, the stability of 2~4 layers is clearly higher than that of a single layer. Therefore, a two-IrO_2-layer/TiO_2 model is employed in our study, considering its favorable stability, electronic structure properties, and the efficient use of precious Ir. Notably, multiple interfacial active sites can coexist, including IrO_2/TiO_2 boundary sites or dual-interface sites involving both solids and liquid. Although these configurations may affect reaction pathways and selectivity, systematically accounting for all possible interfacial geometries would be computationally prohibitive and is beyond the scope of this work. Future studies may address these effects in greater detail.

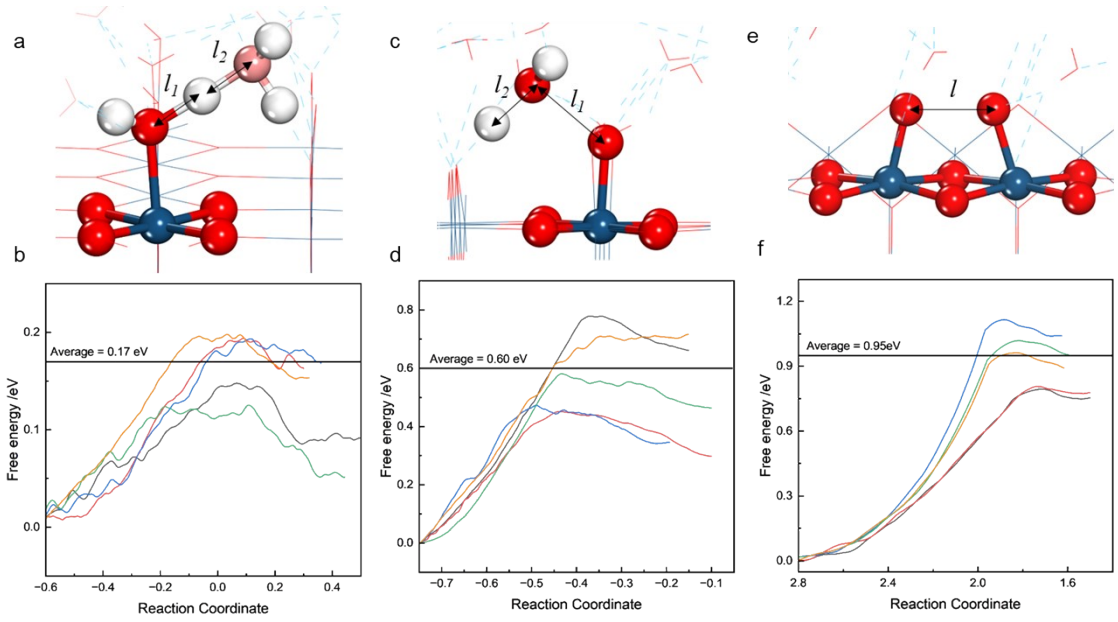

Figure S2. (a) The definition of the reaction coordinate, equal to the difference between O-H bond distance l_1 in H_2O and the H-O bond distance l_2 in the nearest H_2O. (b) Energy profiles of H_2O dissociation process at $H_2O/IrO_2/TiO_2$ interface using the slow-growth method. (c) The definition of the reaction coordinate, equal to the difference between H-O bond distance l_1 in H_2O and the O-O distance l_2. (d) Energy profiles of WNA process at aqueous IrO_2/TiO_2 interface using the slow-growth method. (e) The definition of the reaction coordinate, equal to the difference of O-O bond (l). (f) Energy profiles of I2M at $H_2O/IrO_2/TiO_2$ interface using the slow-growth method.

Notes: The slow-growth based AIMD method is an effective way for calculating free energy profiles and has been successfully applied to capture the evolution of hydrogen-bonding networks during aqueous reactions.[23-27] In this method, the reaction coordinate (ξ) is varied linearly from state 1 to state 2 with a constant and sufficiently small transformation velocity ($\dot{\xi}$). The corresponding free energy difference is obtained as:

$$\Delta F_{1\to 2} = \int_{\xi 1}^{\xi 2} \left(\frac{\partial F}{\partial \xi}\right)_{\xi *} d\xi = \lim_{\dot{\xi}\to 0} \int_{\xi 1}^{\xi 2} \left(\frac{\partial F}{\partial \xi}\right) \cdot \dot{\xi} dt \qquad \text{(S12)}$$

where F is the free energy at the coordinate ξ evolving with time t, and $\partial F/\partial \xi$ is evaluated along the MD trajectory using the SHAKE algorithm.[28] Notably, using this method, we calculated the energetics of water dissociation and O–O bond formation via both the I2M and WNA pathways. For the water dissociation, the collective variable (CV) was defined as $\xi=l_1-l_2$ (the difference between O-H bond distance l_1 in H_2O and the H-O bond distance l_2 in the nearest H_2O, as illustrated in Figure S2a). A small increment of 0.001 Å per MD step was applied in practice. The slow-growth approach was implemented using the VASP code, and the integrated free energy profiles

are shown in Figure S2b. To ensure statistical reliability for the aqueous system, multiple slow-growth simulations were performed starting from different initial configurations. Specifically, five independent trajectories were calculated and averaged. The resulting free energy barrier for the water dissociation is 0.17 eV, in excellent agreement with the value obtained from the MPA-MD method (0.18 eV). Similarly, the collective variable (CV) of WNA process was defined as $\xi=l_1-l_2$ (the difference between H-O bond distance l_1 in H_2O and the O-O distance l_2, as illustrated in Figure S2c). The result shows that the free energy barrier is 0.60 eV, which is in good agreement with the value obtained from the MPA-MD method (0.53 eV). For the I2M mechanism, the collective variable was defined as the O-O bond length ($\xi=l$, Figure S2e), and the free energy barrier was calculated to be 0.95 eV (Figure S2f), which is also close to the value obtained from the MPA-MD method (0.89 eV). These results further demonstrate the reliability of our model and methodology for describing OER at the /IrO_2/TiO_2 interface.

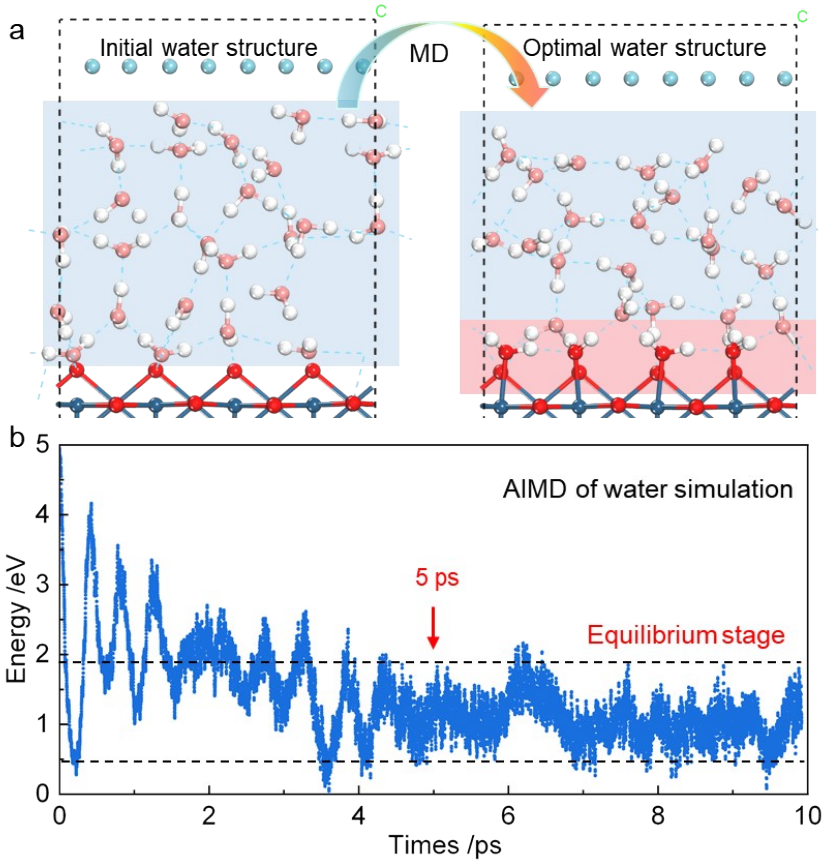

Figure S3. (a) Initial and optimal water structures over solid surface applied to AIMD simulation of H_2O/IrO_2/TiO_2 interface. (b) The corresponding energy profile of AIMD simulation duration of 0-10 ps at H_2O/IrO_2/TiO_2 interface.

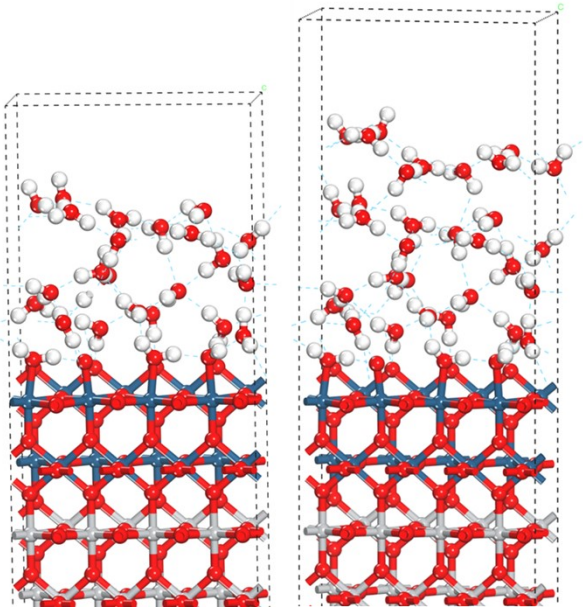

Figure S4. The structure of aqueous IrO_2/TiO_2 model with 26 and 35 water molecules explicitly introduced.

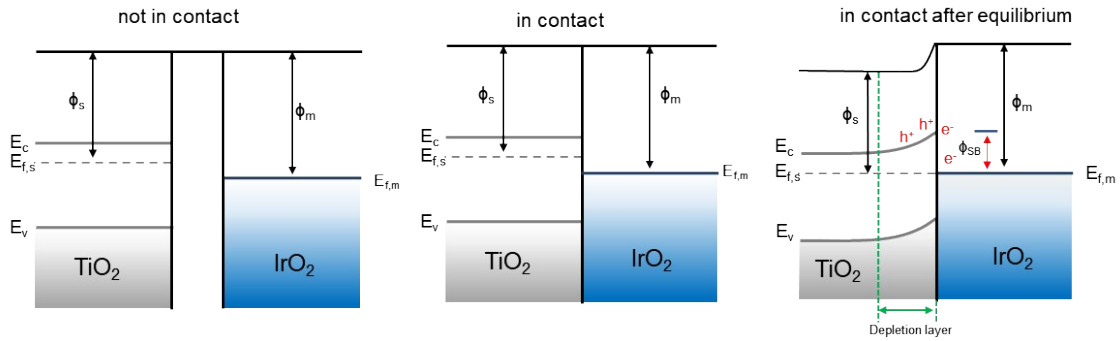

Figure S5. Schematic illustration of upward band bending of IrO_2/TiO_2 heterostructure.

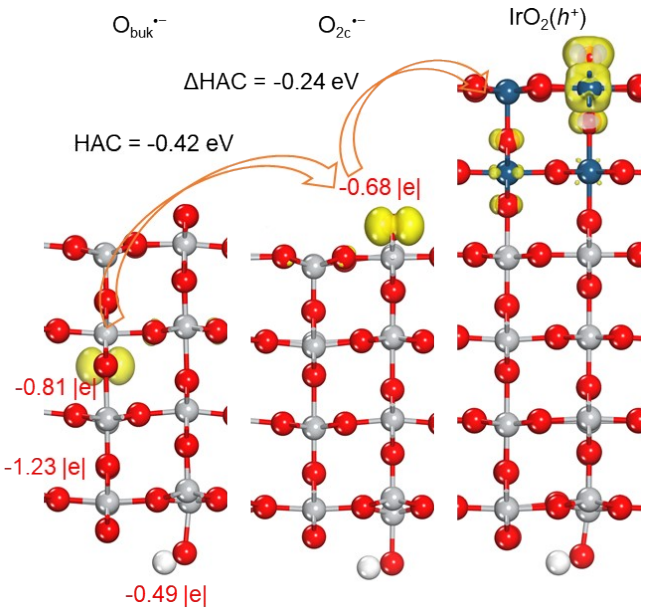

Figure S6. The spin density plots (isovalue = 0.005 e/Å3) of one photo-hole trapped in the bulk of TiO_2 catalyst, surface O_{2c} site of TiO_2(110), and IrO_2 layer of IrO_2/TiO_2 system, respectively.

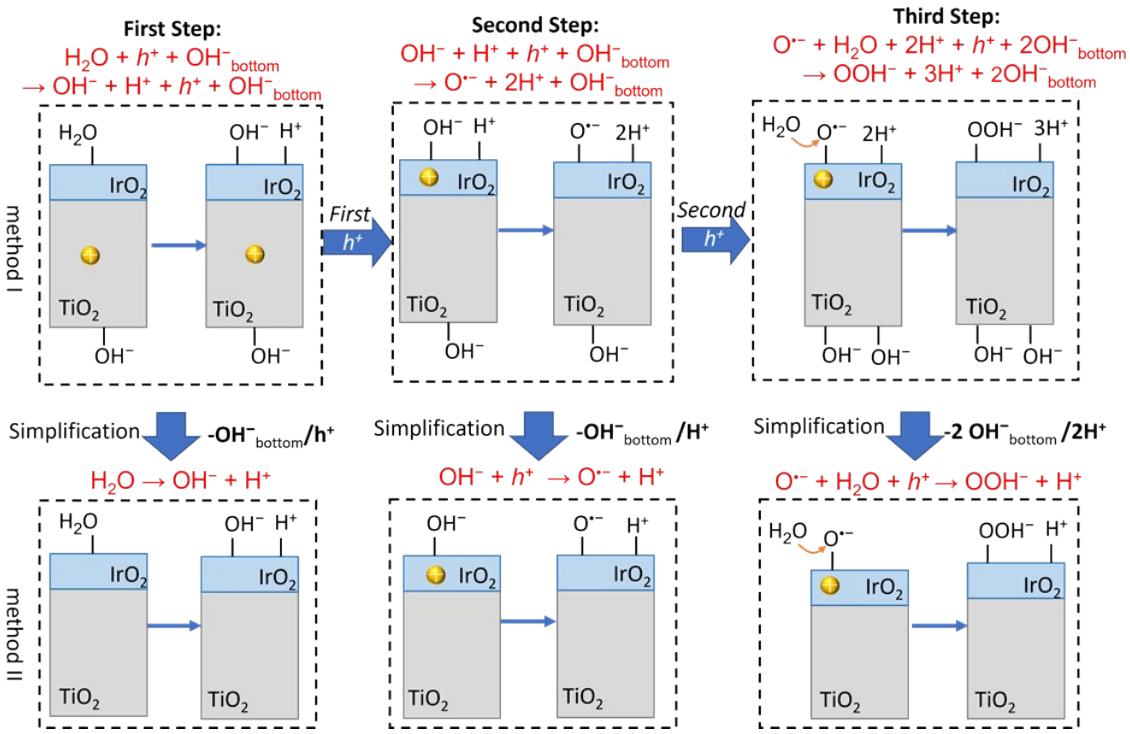

Figure S7. Scheme of the hole simulation during the different reaction stage.

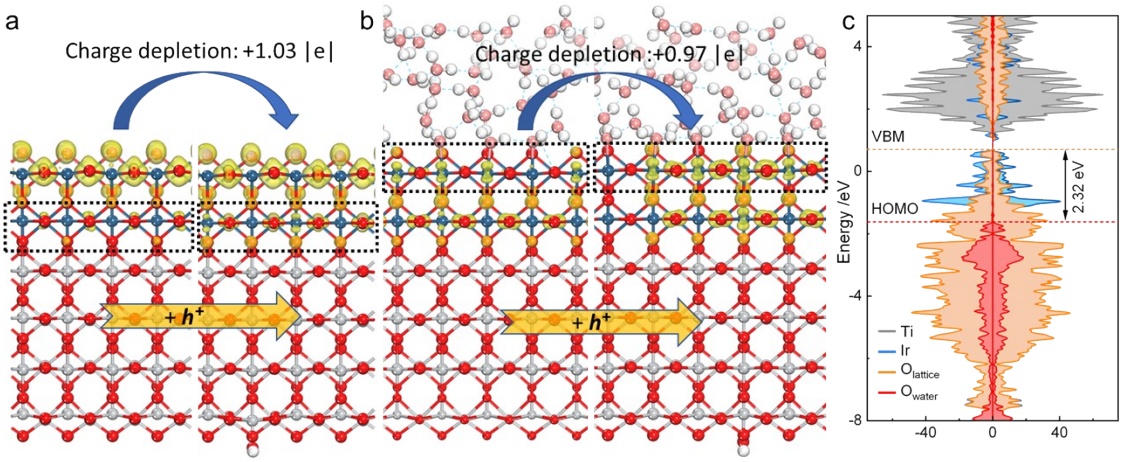

Figure S8. (a) Spin density of IrO_2/TiO_2 without and with h^+ present under gas-phase conditions. (b) Spin density of IrO_2/TiO_2 without and with h^+ present under explicit aqueous conditions. (c) The PDOS of $H_2O/IrO_2/TiO_2$ with VBM of IrO_2/TiO_2 and highest occupied molecular orbital (HOMO) of H_2O molecules marked.

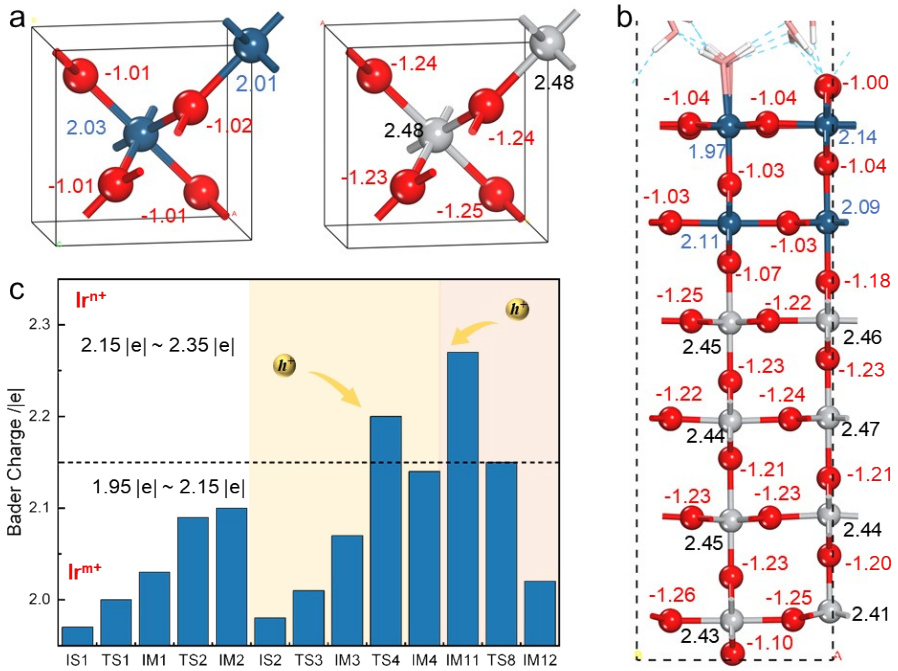

Figure S9. (a) Bader charge of bulk IrO_2 and TiO_2. (b) Bader charge of the aqueous IrO_2/TiO_2 interface, where the Bader charges of Ir, Ti and O are marked by blue, black and red, respectively (unit: |e|). (c) The Bader charge of Ir involved in the key initial state (IS), transition state (TS) and intermediate state (IM) structures for OER.

Note: For the determination of Ir oxidation state, it is important to emphasize that Bader charge

analysis provides non-integer, non-normalized values; therefore, the resulting charges should not be interpreted as exact formal oxidation states. As a benchmark, our Bader analysis indicates that the Ir atoms in bulk IrO_2 have the charge of approximately +2.03 |e| (Figure S9a), which is lower than that of Ti in TiO_2 (+2.48 |e| for Ti^{4+}), highlighting the challenge of directly correlating Bader charges with formal oxidation states. At the aqueous IrO_2/TiO_2 interface, the Bader charges of Ir atoms under different coordination environments range from +1.97 |e| to +2.14 |e| (Figure S9b). Upon h^+ introduction, IrO_2 exhibits metallic-like behavior, leading to delocalization of the hole and negligible change in the Bader charges of individual Ir atoms. Specifically, the Ir charges remain within the range of +1.95 |e| to +2.15 |e| (Figure S9c) before and after hole injection, while the total integrated spin density confirms the addition of one hole (+1.0 |e|) (Figure 1b, main text). This behavior contrasts sharply with TiO_2, where h^+ localization induces substantial shifts in O Bader charges from -1.23 |e| to -0.68 |e| (Figure S6).

Nevertheless, in specific surface reactions where strong h^+ localization occurs (e.g., upon adsorption of an $O^{\bullet-}$ radical), the valence state of the $O^{\bullet-}$-bound Ir atom increases significantly, reaching approximately +2.35 |e| (see Figure S9c). To describe these subtle valence changes without implying misleading formal charges, we adopt a letter-based indexing notation in the manuscript: Ir atoms with Bader charge between +1.95 |e| and +2.15 |e| are denoted as +*m*, while Ir atoms with charges from +2.15 |e| to +2.35 |e| are denoted as +*n*. This nomenclature follows the conventions adopted in previous studies. For example, Nong et al.[28] designated Ir sites with trapped h^+ as Ir^{N+}, and described adjacent oxygen atoms as $O^{(II-\delta)-}$. Similarly, Cheng et al.[29] employed Mulliken charge analysis to characterize the electronic structure of Ir, highlighting the importance of using charge partitioning methods rather than relying strictly on formal oxidation states.

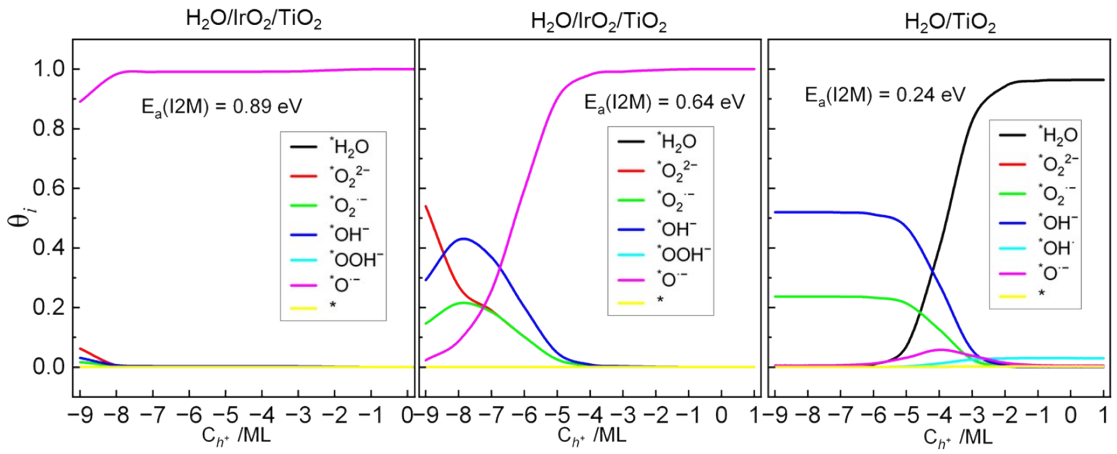

Figure S10. The coverage changes of the reactant and intermediates with increasing C_{h+} at the $H_2O/IrO_2/TiO_2$ and the H_2O/TiO_2 interfaces.

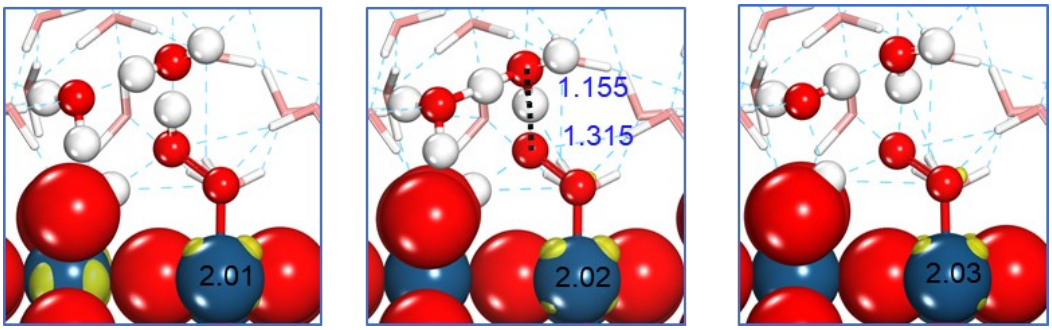

Figure S11. The spin density plot of IS, TS and FS of deprotonation of $^*OOH^-$ at the $H_2O/IrO_2/TiO_2$ interface. The bond lengths of the key intermediates as well as the Bader charges of Ir_{5c} sites are marked in blue and black, respectively. Bond length: Å; Bader charge: |e|.

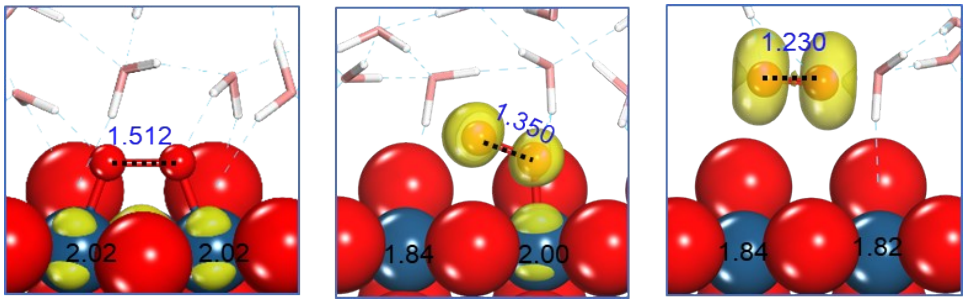

Figure S12. The sequential oxidation of O_2^{2-} by h^+ ($O_2^{2-} \rightarrow O_2^{\bullet-} \rightarrow O_2$) is clearly accompanied by the stepwise decrease in the O-O bond length ($l_{O\text{-}O}$: 1.512 → 1.350 → 1.230 Å) as well as the progressively stretched $l_{O\text{-}O}$ at the $H_2O/IrO_2/TiO_2$ interface, indicating the gradual detachment of an oxygen from the surface. Bond length: Å; Bader charge: |e|.

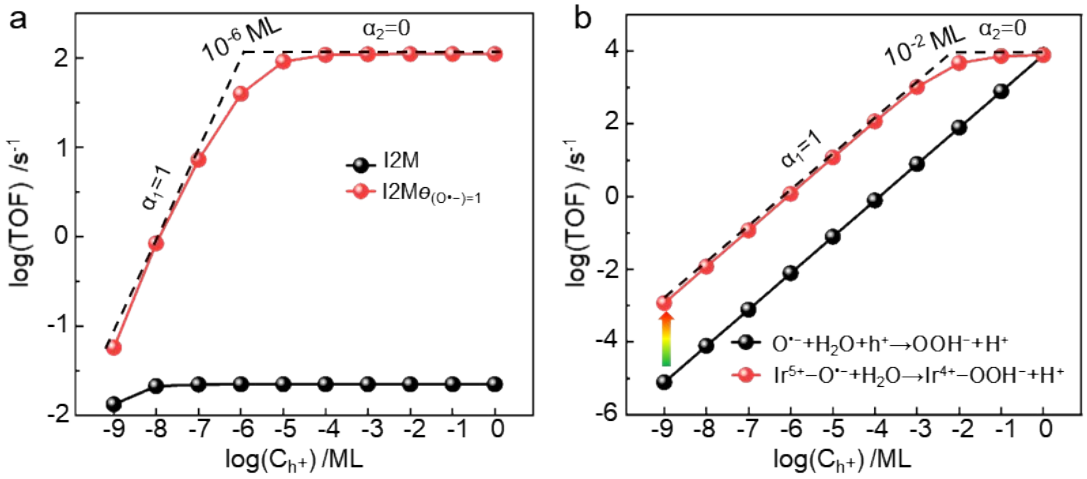

Figure S13. (a) The TOFs of O_2 as a function of C_{h+} by I2M without and with considering the coverage of $O^{\bullet-}$ radical. (b) The TOFs of O_2 as a function of C_{h+} by WNA without and with considering h^+ trapping.

Note: Under the reaction conditions, the I2M is facilitated by the weakened $E_{ads}(O@Ir_{5c})$. We found that the reaction order ($r_{OER} = k_{OER}[C_{h+}]^{\alpha}$, where k_{OER} is the OER rate reaction constant and α is the reaction order with respect to C_{h+}) of the O_2 generation via I2M is 1 at $C_{h+} < 10^{-6}$ ML, implying that the intrinsic catalytic activity of IrO_2/TiO_2 is sufficient, and the primary limitation for overall O_2 generation is the low concentration of surface-reaching holes. By contrast, at C_{h+} $>10^{-6}$ ML, α becomes 0, implying that the TOF is independent of C_{h+}, and thus lowering the barrier of I2M can further increase the TOF. Similarly, α in WNA is 1 at low C_{h+} and 0 at high C_{h+}. However, the turning point is different, which is significantly higher for WNA compared to I2M (10^{-4} vs 10^{-2} ML). This difference arises because, at sufficiently high hole concentrations, WNA, with its lower energy barrier compared to I2M, facilitates the reaction more easily. Once C_{h+} exceeds 10^{-2} ML, the reaction meets kinetics requirements, and the limiting factor for overall catalytic activity becomes the relatively low intrinsic catalytic activity of the catalyst.

The C_{h+}-dependent variation of the reaction order for the O-O bond formation step can also be explained by the reaction rate under steady-state conditions at different C_{h+}. Specifically, taking I2M as an example, under the steady-state condition, the reaction rates of all the steps are determined numerically by solving the following mathematical reactions:

$$\theta(*) + \theta(H_2O) + \theta(OH^-) + \theta(O^{\bullet-}) + \theta(O_2^{2-}) + \theta(O_2^-) = 1 \quad \text{(S12)}$$

$$r_1 = r_2 = r_3 = 2r_6 \quad \text{(S13)}$$

$$r_6 = r_{10} = r_{11} \quad \text{(S14)}$$

The related reaction equations are listed in Table S8. When the reaction reaches equilibrium, the reaction rate of O-O bond formation can be written as:

$$r_{I2M} = r_6 = k_{6+}\theta(O^{\bullet}-)^2(1-Z_6) \quad \text{(S15)}$$

According to the calculated results, Z_6 is far less than 1 at C_{h+} of $10^{-9} - 10^{0}$ ML, and the reaction rate is determined by $\theta(O^{\bullet-})$. The relationship between $\theta(O^{\bullet-})$ and C_{h+} can be written as:

$$\left[\frac{2k_{6+}(1-Z_6)}{k_{1+}C_{H_2O}(1-Z_1)} + \frac{2k_{6+}(1-Z_6)}{k_{2+}(1-Z_2)} + \frac{2k_{6+}(1-Z_6)}{k_{3+}C_{h+}(1-Z_3)} + \frac{2k_{6+}(1-Z_6)}{k_{10+}C_{h+}(1-Z_{10})} + \frac{2k_{6+}(1-Z_6)}{k_{11+}C_{h+}(1-Z_{11})} + \right] \theta(O^{\cdot-})^2 + \theta(O^{\cdot-}) = 1 \quad \text{(S16)}$$

In Eq-S16, k_{6+} is much lower than k_{1+}, k_{2+}, k_{3+}, k_{10+}, k_{11+} (referred to Table S8) and Z_1, Z_2, Z_3, Z_{11} are much less than 1 (see Table S8), and then the relationship can be simplified as:

$$\left[\frac{2k_{6+}}{k_{3+}C_{h+}} + \frac{2k_{6+}}{k_{10+}C_{h+}} + \frac{2k_{6+}}{k_{11+}C_{h+}}\right]\theta(O^{\cdot-})^2 + \theta(O^{\cdot-}) = 1 \quad \text{(S17)}$$

When C_{h+} is low, the $\theta(O^{\bullet-})$ is related to C_{h+}. However, as C_{h+} increases, the first term in the Eq-S17 approaches 0 and $\theta(O^{\bullet-})$ approaches 1. As shown in Figure S13a and b, the microkinetic result shows that with C_{h+} increasing, $\theta(O^{\bullet-})$ increases and then remains constant, resulting in a change of the reaction order of I2M with respect to C_{h+} from 1 to 0.

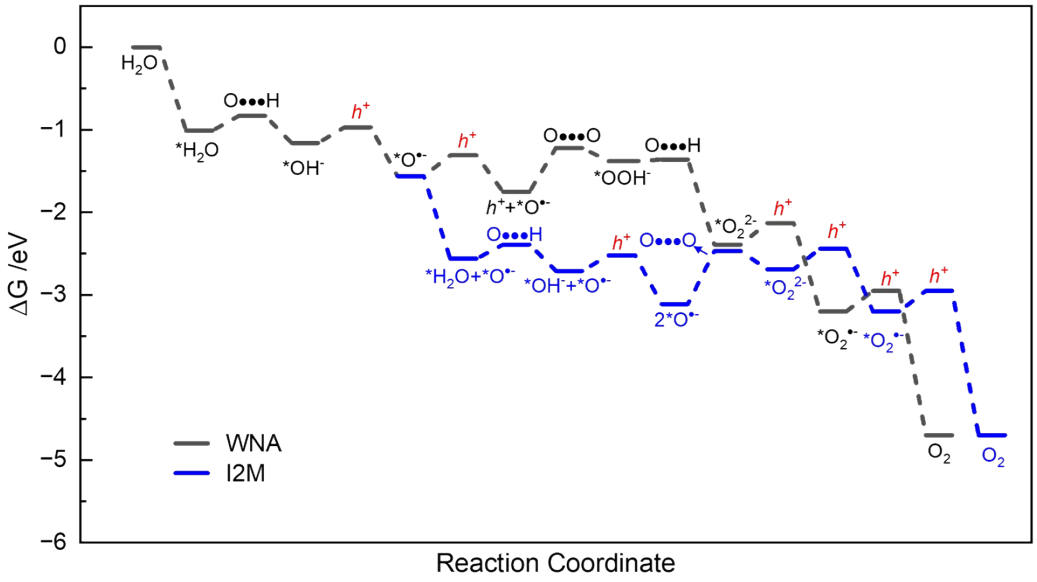

Figure S14. The energy profiles of photocatalytic OER mechanism at the H_2O/TiO_2 interface.

Notes: The OER mechanism at the $H_2O/IrO_2/TiO_2$ interface is illustrated in Figure S14 and Figure 5a of the main text. The reaction begins with the deprotonation of adsorbed water molecules to generate OH^-, followed by the trapping of a h^+ to form an $OH^\bullet$ radical on the surface. Then, the $OH^\bullet$ deprotonates readily, yielding an $O^{\bullet-}$ radical. After coupling with a nearby $O^{\bullet-}$, two successive h^+ can oxidize the as-formed $(O\text{-}O)^{2-}$ species to form O_2.

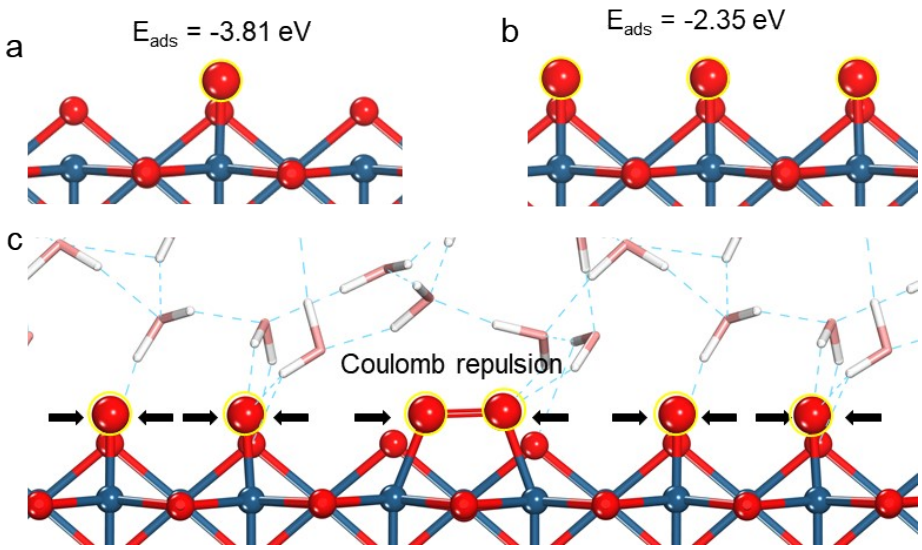

Figure S15. (a and b) Optimized adsorption structures and energies of $^{*}O^{\bullet-}$ intermediate on bare IrO_2/TiO_2 and oxygen-covered surface, respectively. (c) The TS of O-O bond formation by I2M on the oxygen-covered IrO_2/TiO_2 surface.

Notes: As the OER reaches steady state, self-evolved O atoms accumulate along the Ir_{5c} sites at the $H_2O/IrO_2/TiO_2$ interface (Figure S15a). Consequently, the barrier of the O-O coupling step decreases, due to the Coulomb repulsion between the $O^{\bullet-}$ radicals, making the O atoms more reactive and facilitating their combination. This effect is also reflected in the reduced O-Ir_{5c} bond strength on the O-covered IrO_2/TiO_2 surface (E_{ads}(O)= -2.35 eV vs. -3.81 eV). As a result, the overall TOF of the IrO_2/TiO_2 catalyst is significantly enhanced when coverage effects are considered.

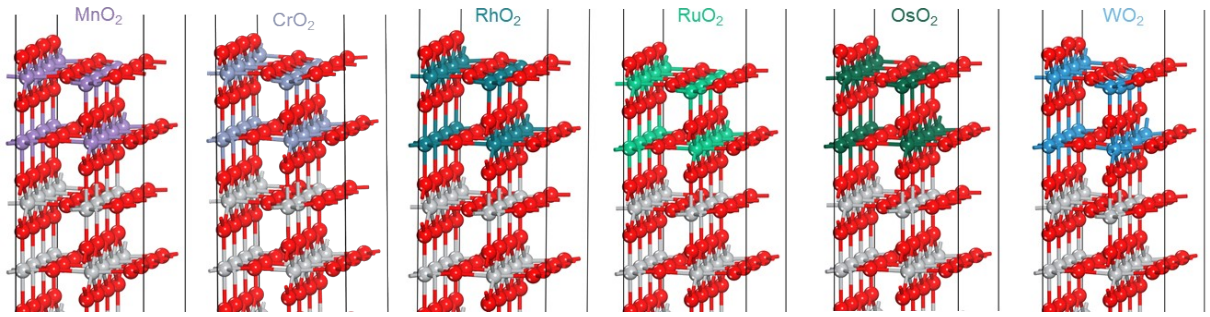

Figure S16. Side views of the rutile-MO_2/TiO_2(110) catalysts (M=Mn, Cr, Rh, Ru, Os and W).
Notes: To model MO_2/TiO_2, both layers of IrO_2 are replaced by the metal M and further optimized. The resulting MO_6 octahedrons are slightly distorted and connected to each other through shared vertices to form the rutile structure. The lattice constants of bulk MO_2 and TiO_2 indicate that the lattice mismatch for all supported catalysts is below 5% along the (110) direction (Table S3). Because both components adopt the same rutile crystal structure, there are no dangling bonds at the MO_2/TiO_2 interface. In other words, the coordination numbers of all atoms are fully saturated, as in the bulk phase.

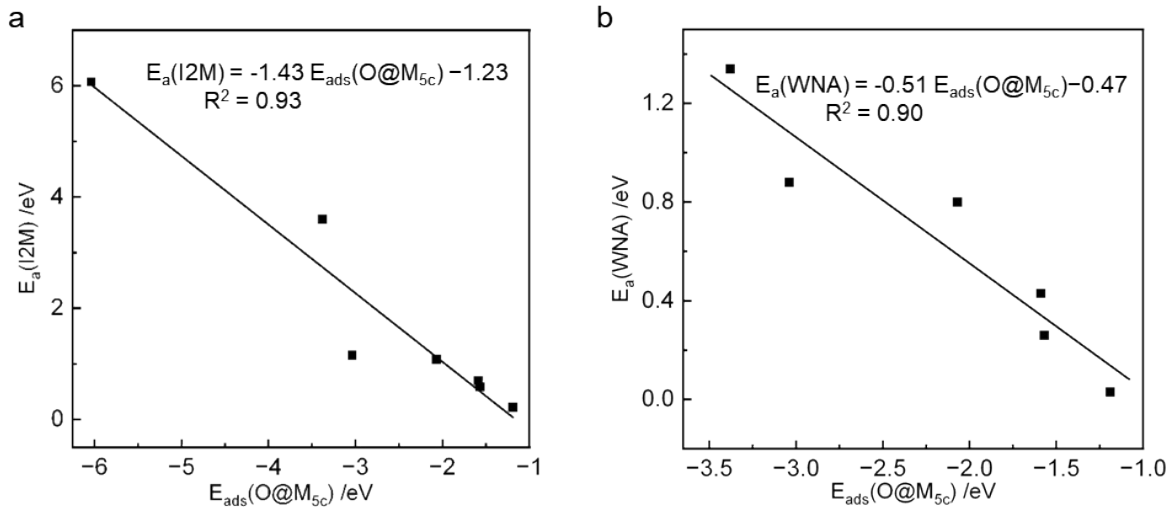

Figure S17. The variation of the calculated E_a(I2M) (a) and E_a(WNA) (b) with different E_{ads}(O@M_{5c}).

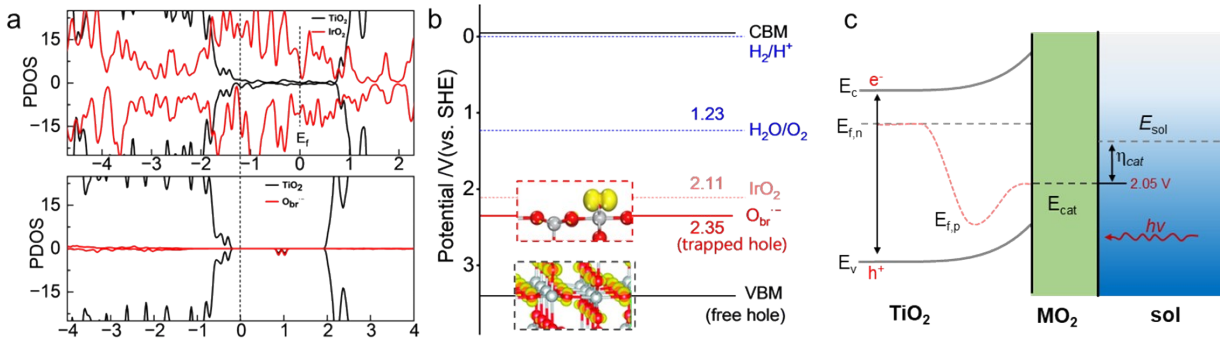

Figure S18. (a) PDOSs of TiO_2 with a hole trapped at O_{br} and IrO_2/TiO_2 with a hole accumulated at IrO_2 sites. (b) Energy levels of the VBM and CBM of TiO_2(110), together with the redox potentials of $4H^+ + 4e^- \rightarrow 2H_2$, $O_2 + 4H^+ + 4e^- \rightarrow 2H_2O$ reactions, and the trap-state energy level of hole localized on O_{br} and IrO_2 sites. Insets show the spin-density distributions (isovalue = 0.005 e/Å^3) of a photoexcited hole delocalized in the bulk of TiO_2 catalyst and trapped at the surface O_{2c} site of TiO_2(110), respectively. (c) Schematic quasi-Fermi levels for illuminated cocatalyst-modified n-type semiconductor TiO_2 systems (MO_2/TiO_2) under quasi-equilibrium conditions.

Notes: In photocatalytic OER systems, the effective driving force is determined by the energy level and concentration of photogenerated holes, which can be described by quais-Fermi level of holes (E_{Fp}).[30-33] Here, we also estimated the quais-Fermi level of holes for the TiO_2 system to understand effect of the thermodynamical driving force on modulating the OER activity trend. According to the semiconductor theory, the hole quasi-Fermi level of TiO_2 can be expressed as:

$$E_{F_p} = E_V + k_B T ln(\frac{p}{N_v}) \quad \text{(S18)}$$

where E_V is the valence-band maximum, p is the hole concentration, and N_v is the effective density of states. Using representative values reported for TiO_2 photocatalytic systems (N_v is 10^{17}-10^{19} cm^{-3}; the free hole concentration p is 10^{12}-10^{17} cm^{-3}),[34, 35] the estimated E_{Fp} for free holes (>2.93 eV vs SHE) remains largely more positive than the OER redox potential (1.23 V vs SHE), indicating a sufficiently large thermodynamic driving force for water oxidation, consistent with a common point that the VBM of TiO_2 is sufficiently deep to place the hole quasi-Fermi level far above the OER potential.

In parallel, the effective quasi-Fermi level associated with surface-trapped holes (commonly existing at $O_{br}^{\bullet-}$ on TiO_2 surface), which are more directly involved in the OER process as longer-lived oxidative species following energy dissipation (with the trap-state energy level $E_{trap}(O_{br}^{\cdot-})$ being 2.35 V vs SHE; Figure S18b), was evaluated to be ~2.05 V (Figure S18c) based on experimental surface-localized hole concentration (~10^{17} cm^{-3} under typical illumination intensity).[35] This E_{Fp} still remains more positive than the OER redox potential. For cocatalyst-loaded systems, when considering the quasi-equilibrium approximation, the Fermi level of the

metallic-like cocatalyst aligns with the hole quasi-Fermi level in TiO_2 photocatalyst under illumination conditions (Figure S18c), consistent with previous studies.[30, 31] In this quasi-equilibrium framework, cocatalysts with lower trapped-hole energy levels (Figure S18b) can accommodate higher hole populations according to the Fermi–Dirac/Boltzmann distribution, thereby enhancing hole accumulation within the cocatalyst region. Beyond the quasi-equilibrium approximation, cocatalyst loading can facilitate spatial charge separation and suppress electron-hole recombination, which may lead to additional positive shifts of the quasi-Fermi level relative to the solution redox potential under realistic nonequilibrium conditions, although a rigorous quantitative description would require explicit treatment of charge transport and nonequilibrium carrier dynamics, which is beyond the scope of the present work.

Taken together, these quasi-Fermi-level discussions suggest that the present photocatalytic system possesses a sufficiently strong thermodynamic driving force for water oxidation, thereby providing a qualitative explanation for the observed shift in the volcano-type activity trend in comparison with the electrocatalytic OER systems (working at typical overpotentials of ~0.3 V), analogous to the shift observed for optimal hydrogen binding at high driving-force conditions.[36]

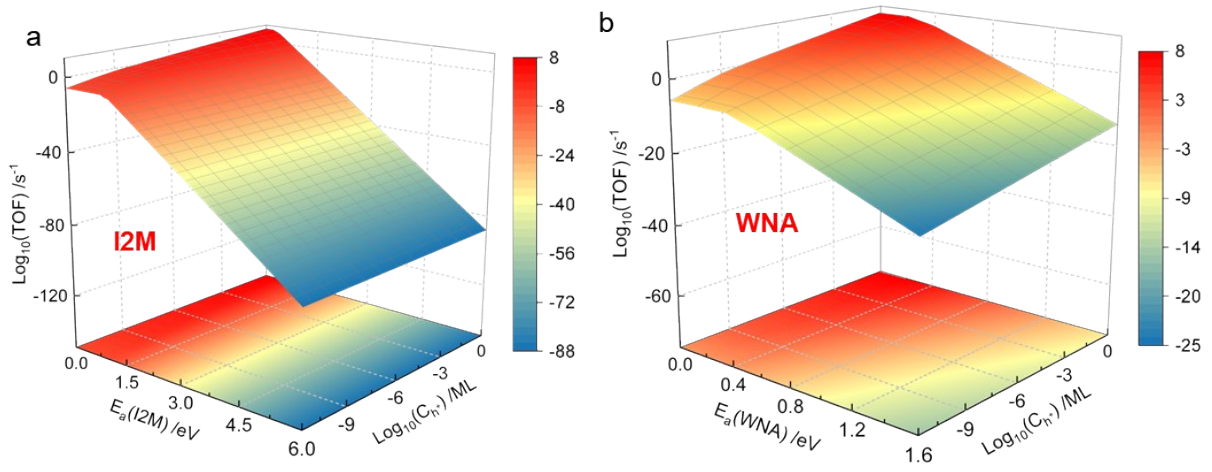

Figure S19. TOF of product O_2 as a function of the E_a(I2M) (a) and E_a(I2M) (b) with C_{h+} on MO_2/TiO_2 (M = Mn, Cr, Rh Ru, Ir, Os and W).

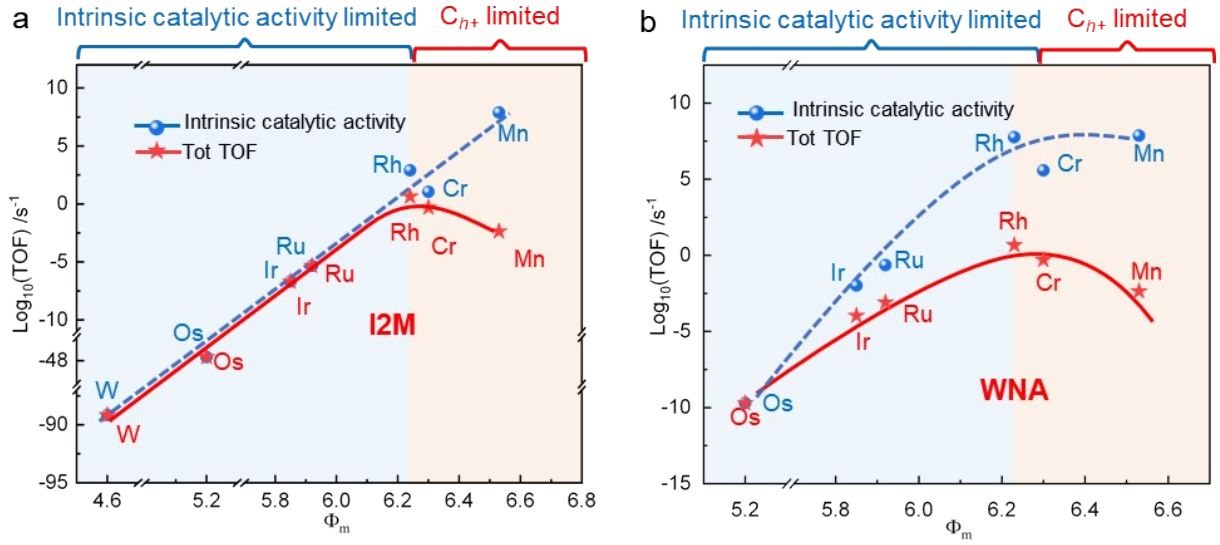

Figure S20. (a) The volcano-typed activity trend and the trend of the intrinsic catalytic activity with the O-O bond formation by I2M as ϕ_m changes. (b) The volcano-typed activity trend and the trend of the intrinsic catalytic activity with the O-O bond formation by both I2M and WNA as ϕ_m changes.

Table S1. Comparison of the energetic results of O-O bond formation via WNA using cutoff energies of 450 and 500 eV

	IS /eV		FS /eV		ΔE /eV	
	450 eV	500 eV	450 eV	500 eV	450 eV	500 eV
1	-703.84	-703.34	-703.23	-702.67	0.61	0.67
2	-703.65	-703.16	-703.27	-702.64	0.38	0.57
3	-703.46	-702.89	-703.05	-702.70	0.41	0.19
4	-704.24	-703.71	-703.87	-703.24	0.37	0.47
5	-704.73	-703.98	-704.34	-703.53	0.39	0.45

Table S2. Comparison the energetic results of O-O coupling with U of 5.25 and 6.3 eV.

	E_a /eV		ΔH /eV	
	U=5.25 eV	U=6.3	U=5.25	U=6.3
$O^{\bullet-}$/ $O^{\bullet-}$	0.89	0.79	0.62	0.60

Table S3. Comparison of O-O bond formation energies via WNA with 26 and 35 water molecules explicitly introduced.

	E_a /eV		ΔH /eV	
	26	35	26	35
WNA	0.53	0.62	0.37	0.44

Table S4. The lattice parameter of bulk MO_2 (M= Mn, Cr, Rh Ru, Ir, Os and W) and TiO_2 with the corresponding lattice mismatch when MO_2 loaded on TiO_2(110).

MO_2	a /Å	b /Å	c /Å	(110) surface Lattice mismatch
TiO_2	4.594	4.594	2.959	—
MnO_2	4.400	4.400	2.867	4%
CrO_2	4.409	4.409	2.914	4%
RhO_2	4.487	4.487	3.090	2%
RuO_2	4.483	40483	3.111	2%
IrO_2	4.505	4.505	3.177	2%
OsO_2	4.478	4.478	3.209	3%
WO_2	4.837	4.805	3.213	5%

Table S5. Bader charge (denoted as C, in |e|) of the M site (M=Ir_{5c} or Ti_{5c}) and adsorption energy (E_{ads}, in eV) of some key intermediates ($^*H_2O$, $^*OH$ and $^*O$) at the H_2O/TiO_2 and $H_2O/IrO_2/TiO_2$ interfaces.

Intermediates		H_2O/TiO_2		$H_2O/IrO_2/TiO_2$	
		neutral	hole	neutral	hole
clean	C_M	2.39	2.39	1.84	1.85
$^*H_2O$	C_M	2.40	2.40	1.97	1.98
	E_{ads}	-0.74	-0.74	-1.45	-0.85
$^*OH$	C_M	2.46	2.44	2.03	2.07
	E_{ads}	-2.52	-0.99	-2.84	-2.80
$^*O$	C_M	2.39	2.45	2.10	2.14
	E_{ads}	-2.61	-1.38	-3.68	-3.04

Table S6. Reaction energetics of each elementary step at the $H_2O/IrO_2/TiO_2$ and H_2O/TiO_2 interfaces for the microkinetic modeling.

		$H_2O/IrO_2/TiO_2$		H_2O/TiO_2	
No.	Elementary steps	E_a/eV	ΔG/eV	E_a/eV	ΔG/eV
1	$H_2O + {}^* \rightarrow {}^*H_2O$	0.00	-1.02	0.00	-0.16
2	$^*H_2O \rightarrow {}^*OH^- + H^+$	0.18	-0.15	0.50	0.24
3	$^*OH^- + h^+ \rightarrow {}^*O^{\bullet-} + H^+$	0.19	-0.40	—	—
4	$^*OH^- + h^+ \rightarrow {}^*OH^\bullet$	—	—	0.25	-0.20
5	$^*OH^\bullet \rightarrow {}^*O^{\bullet-} + H^+$	—	—	0.41	-0.53
6	$^*O^{\bullet-} + {}^*O^{\bullet-} \rightarrow {}^*O_2^{2-}$	0.89(0.64)	0.62(0.42)	0.24	-0.21
7	$^*O^{\bullet-} + h^+ \rightarrow {}^\#O^{\bullet-}$	0.25	-0.19	—	—
8	$^\#O^{\bullet-} + H_2O \rightarrow {}^*OOH^- + H^+$	0.53	0.37	—	—
9	$^*OOH^- \rightarrow {}^*O_2^{2-} + H^+$	0.02	-1.01	—	—
10	$^*O_2^{2-} + h^+ \rightarrow {}^*O_2^{\bullet-}$	0.25	-0.51/-0.83[a]	0.25	-1.82
11	$^*O_2^{\bullet-} + h^+ \rightarrow O_2 + {}^*$	0.25	-1.40	0.25	-2.45

All the results are calculated using our MPA-MD method except for the h^+ diffusion barrier. * represents Ir^{m+} and $^\#$ represents Ir^{n+} on the IrO_2/TiO_2 surface. * represents Ti^{4+} on pristine TiO_2. [a]The exothermic energy of hole trapping for the $^*O_2^{2-}$ intermediate formed via the I2M and WNA mechanisms, respectively.

Table S7. Coverage (θ_i) and degree of thermodynamic rate control (TRC) of key intermediates at the $H_2O/IrO_2/TiO_2$ and H_2O/TiO_2 interfaces at $C_{h+} = 10^{-5}$ ML and $C_{h+} = 10^{-9}$ ML, respectively.

	$H_2O/IrO_2/TiO_2$		H_2O/TiO_2	
Species	θ_i	TRC	θ_i	TRC
$^*OH^-$	4.82×10^{-2}	-8.36×10^{-2}	5.20×10^{-1}	-5.00×10^{-1}
$^*O^{\bullet-}$	9.00×10^{-1}	-1.56×10^{0}	5.32×10^{-3}	-4.29×10^{-2}
$^*OH^{\bullet}$	—	—	2.31×10^{-7}	-2.22×10^{-7}
$^*O_2^{2-}$	2.54×10^{-2}	-4.41×10^{-2}	2.37×10^{-1}	-2.28×10^{-1}
$^*O_2^-$	2.54×10^{-2}	-4.41×10^{-2}	2.37×10^{-1}	-2.28×10^{-1}
$^*OOH^-$	1.71×10^{-12}	-2.97×10^{-12}	—	—

Table S8. Reaction rate equations for each elementary step of photocatalytic OER and corresponding reaction rates (r_i), reversibility (Z_i) and the degree of rate control (DRC) of elementary step i at the $H_2O/IrO_2/TiO_2$ and H_2O/TiO_2 interfaces at $C_{h+} = 10^{-5}$ ML and $C_{h+} = 10^{-9}$ ML, respectively.

No.	Reaction rate equations	$H_2O/IrO_2/TiO_2$			H_2O/TiO_2		
		r_i/s^{-1}	Z_i	DRC	r_i/s^{-1}	Z_i	DRC
1	$r_1=k_{1+}\cdot C_{H2O}\cdot\theta(*)\cdot(1-Z_1)$	1.90×10^{2}	2.30×10^{-18}	7.99×10^{-6}	1.87×10^{-1}	1.00×10^{0}	2.16×10^{-11}
2	$r_2=k_{2+}\cdot\theta(^{*}H_2O)\cdot(1-Z_2)$	1.90×10^{2}	9.46×10^{-6}	3.52×10^{-12}	1.87×10^{-1}	9.96×10^{-1}	1.86×10^{-5}
3	$r_3=k_{3+}\cdot C_{h+}\cdot\theta(^{*}OH^{-})\cdot(1-Z_3)$	1.90×10^{2}	7.58×10^{-9}	3.66×10^{-5}	–	–	–
4	$r_4=k_{4+}\cdot C_{h+}\cdot\theta(^{*}OH^{-})\cdot(1-Z_4)$	–	–	–	1.87×10^{-1}	8.94×10^{-2}	4.77×10^{-1}
5	$r_5=k_{5+}\cdot\theta(^{*}OH^{\bullet})\cdot(1-Z_5)$	–	–	–	1.87×10^{-1}	2.89×10^{-12}	4.69×10^{-2}
6	$r_6=k_{6+}\cdot\theta(^{*}O^{\bullet-})^{2}\cdot(1-Z_6)$	8.96×10^{1}	1.06×10^{-5}	7.36×10^{-1}	9.34×10^{2}	1.00×10^{0}	1.51×10^{-8}
7	$r_7=k_{7+}\cdot C_{h+}\cdot\theta(^{*}O^{\bullet-})\cdot(1-Z_7)$	1.07×10^{1}	9.97×10^{-1}	2.71×10^{-4}	–	–	–
8	$r_8=k_{8+}\cdot\theta(^{\#}O^{\bullet-})\cdot C_{H2O}\cdot(1-Z_8)$	1.07×10^{1}	2.05×10^{-10}	9.22×10^{-2}	–	–	–
9	$r_9=k_{9+}\cdot\theta(^{*}OOH^{-})\cdot(1-Z_9)$	1.07×10^{1}	1.60×10^{-14}	2.19×10^{-11}	–	–	–
10	$r_{10}=k_{10+}\cdot C_{h+}\cdot\theta(^{*}O_2^{2-})\cdot(1-Z_{10})$	1.00×10^{2}	2.71×10^{-4}	4.41×10^{-2}	9.34×10^{-2}	2.66×10^{-22}	2.39×10^{-1}
11	$r_{11}=k_{11+}\cdot C_{h+}\cdot\theta(^{*}O_2^{-})\cdot(1-Z_{11})$	1.00×10^{2}	3.62×10^{-35}	4.41×10^{-2}	9.34×10^{-2}	7.47×10^{-44}	2.37×10^{-1}

Table S9. Entropy (TΔS) and zero-point-energy (ΔZPE) changes of H_2O adsorption (step 1) and O_2 desorption (step 11).

steps	TΔS	ΔZPE
1	-0.23	0.01
11	0.63	-0.03

Table S10. The E_a(I2M), E_a(WNA), E_{ads}(O@M_{5c}), HAC, C_{h+} and work function (ϕ_m) of MO_2/TiO_2 calculated in the gas phase.

MO_2	E_a(I2M) /eV	E_a(WNA) /eV	E_{ad}(O@M_{5c}) /eV	HAC /eV	C_{h+} /ML^{-1}	ϕ_m /eV
MnO_2	0.22	0.03	-1.19	-0.43	1.47×10^{-9}	6.53
CrO_2	0.70	0.43	-1.59	-0.47	4.91×10^{-9}	6.30
RhO_2	0.59	0.26	-1.57	-0.52	4.70×10^{-8}	6.24
RuO_2	1.08	0.80	-2.07	-0.60	1.06×10^{-6}	5.92
IrO_2	1.16	0.88	-3.04	-0.66	1.0×10^{-5}	5.85
OsO_2	3.60	1.34	-3.38	-1.11	1	5.20
WO_2	6.07	/	-6.04	-1.39	1	4.60

Table S11. Reaction energetics (unit: eV) of each elementary step at the MO_2/TiO_2 interfaces used for microkinetic modeling.

		MnO_2/TiO_2		CrO_2/TiO_2		RhO_2/TiO_2		RuO_2/TiO_2		IrO_2/TiO_2		OsO_2/TiO_2		WO_2/TiO_2	
No.	Elementary steps	E_a	ΔG	E_a	ΔG	E_a	ΔG	E_a	ΔG	E_a	ΔG	E_a	ΔG	E_a	ΔG
1	$H_2O + {}^* \rightarrow {}^*H_2O$	/	-0.26	/	-1.07	/	-1.00	/	-0.98	/	-1.33	/	-1.61	/	-2.89
2	${}^*H_2O + h^+ \rightarrow {}^*O^{\bullet-} + 2H^+$	/	-0.45	/	-0.56	/	-0.71	/	-0.85	/	-0.73	/	-1.37	/	-1.25
3	${}^*O^{\bullet-} + {}^*O^{\bullet-} \rightarrow {}^*O_2^{2-}$	0.22	-1.00	0.70	0.50	0.59	0.40	1.08	0.60	1.16	0.70	3.6	3.12[a]	6.07	5.94[b]
4	${}^*O^{\bullet-} + h^+ + H_2O \rightarrow {}^*OOH^- + H^+$	0.03	-1.20	0.26	-1.01	0.26	-0.16	0.80	0.37	0.88	0.36	1.34	1.30	—	—
5	${}^*OOH^- \rightarrow {}^*O_2^{2-} + H^+$	/	-0.51	/	-0.12	/	-1.15	/	-1.63	/	-1.72	/	-1.16	—	—
6	${}^*O_2^{2-} + 2h^+ \rightarrow O_2 + {}^*$	0.25	-2.53	0.25	-2.19	0.25	-1.93	0.25	-1.89	0.25	-1.53	0.25	-2.11	0.25	-2.61

Note: To reduce the high computational cost associated with liquid–solid interface reaction calculations, the reactions on MO_2/TiO_2 were computed under gas-phase conditions. Additionally, the calculations of equilibrium processes were simplified. [a, b]For OsO_2 and WO_2, the final state of O–O bond formation was modeled using a monodentate adsorption configuration, since the strong O–Os and O–W interactions prevent the stabilization of a bidentate adsorption mode on the surface.

Reference

(1) Wang, D.; Sheng, T.; Chen, J.; Wang, H.-F.; Hu, P., Identifying the key obstacle in photocatalytic oxygen evolution on rutile TiO_2. *Nat. Catal.* **2018**, *1*(4), 291-299.

(2) Chen, J.; Jia, M.; Hu, P.; Wang, H., CATKINAS: a large-scale catalytic microkinetic analysis software for mechanism auto-analysis and catalyst screening. *J. Comput. Chem.* **2021**, *42*(5), 379-391.

(3) Lai, Z.; Sun, N.; Jin, J.; Chen, J.; Wang, H.; Hu, P., Resolving the Intricate Mechanism and Selectivity of Syngas Conversion on Reduced $ZnCr_2O_x$: A Quantitative Study from DFT and Microkinetic Simulations. *ACS Catal.* **2021**, *11*(21), 12977-12988.

(4) Yuan, H.; Yang, H.; Hu, P.; Wang, H., Origin of Water-Induced Deactivation of MnO_2-Based Catalyst for Room Temperature NO Oxidation: A First-Principles Microkinetic Study. *ACS Catal.* **2021**, *11*(12), 6835-6845.

(5) Chen, Z.; Mao, Y.; Chen, J.; Wang, H.; Li, Y.; Hu, P., Understanding the Dual Active Sites of the FeO/Pt(111) Interface and Reaction Kinetics: Density Functional Theory Study on Methanol Oxidation to Formaldehyde. *ACS Catal.* **2017**, *7*(7), 4281-4290.

(6) Wang, D.; Jiang, J.; Wang, H.-F.; Hu, P., Revealing the Volcano-Shaped Activity Trend of Triiodide Reduction Reaction: A DFT Study Coupled with Microkinetic Analysis. *ACS Catal.* **2015**, *6*(2), 733-741.

(7) Dumesic, J. A., Analyses of reaction schemes using De Donder relations. *J. Catal.* **1999**, *185*(2), 496-505.

(8) Deskins, N. A.; Dupuis, M., Intrinsic Hole Migration Rates in TiO_2 from Density Functional Theory. *J. Phys. Chem. C* **2009**, *113*(1), 346-358.

(9) Thompson, T. L.; Yates, J. T., Monitoring Hole Trapping in Photoexcited TiO_2(110) Using a Surface Photoreaction. *J. Phys. Chem. B* **2005**, *109*(39), 18230-18236.

(10) Stegelmann, C.; Andreasen, A.; Campbell, C. T., Degree of rate control: how much the energies of intermediates and transition states control rates. *J. Am. Chem. Soc.* **2009**, *131*(23), 8077–8082.

(11) Stegelmann, C.; Andreasen, A.; Campbell, C. T. Degree of rate control: how much the energies of intermediate and transition states control rates. *J. Am. Chem. Soc.* **2009**, *131*(23), 8077-8082.

(12) Wolcott, C.A.; Medford, A. J.; Studt, F.; Campbell, C. T. Degree of rate control approach to computational catalyst screening. *J. Catal.* **2015**, 330, 197-207.

(13) Lide, D.R., CRC Handbook of Chemistry and Physics. *CRC Press, Boca Raton* **2003**,

126(5), 1586-1586.
(14) Wang, D.; Wang, H.; Hu, P. Identifying the distinct features of geometric structures for hole trapping to generate radicals on rutile TiO_2(110) in photooxidation using density functional theory calculations with hybrid functional. *Phys. Chem. Chem. Phys*. 2015, 17, 1549-1555.
(15) Zhang, J.; Peng, C.; Wang, H.; Hu, P. Identifying the role of photogenerated holes in photocatalytic methanol dissociation on rutile TiO_2(110). *ACS Catal.* **2017**, 7, 2374-2380.
(16) Zhou, M.; Wang, H. Optimally selecting photo- and electrocatalysis to facilitate CH4 activation on TiO_2(110) surface: localized photoexcitation versus global electric-field polarization. **2022**, *JACS Au* 2, 188-196.
(17) Ren, G.; Zhou, M.; Hu, P.; Chen, J. F.; Wang, H. Bubble-water/catalyst triphase interface microenvironment accelerates photocatalytic OER via optimizing semi-hydrophobic OH radical. **2024**, *Nat. Commun.* 15, 2346.
(18) Ren, G.; Zhou, M; Wang, H. Weakened Interfacial Hydrogen Bond Connectivity Drives Selective Photocatalytic Water Oxidation toward H_2O_2 at Water/Brookite-TiO_2 Interface. *J. Am. Chem. Soc.* **2024**, 146, 6084-6093.
(19) Ji, Y.; Wang, B.; Luo, Y. Location of trapped hole on rutile-TiO_2(110) surface and its role in water oxidation. *J. Phys. Chem. C* **2012**, 116, 7863-7866.
(20) Jin, F.; Wei, M.; Chen, T.; Ma, H.; Liu, G.; Ma, Y. Behavior of photogenerated electron–hole pair for water splitting on TiO_2(110). *J. Phys. Chem. C* **2018**, 122, 22930-22938.
(21) Ambrosio, F.; Pasquarello, A. Reactivity and energy level of a localized hole in liquid water. *Phys. Chem. Chem. Phys*. **2018**, 20, 30281-30289.
(22) Ma, H.; Feng, J.; Jin, F.; Wei, M.; Liu, C.; Ma, Y. Where do photogenerated holes at the gC_3N_4/water interface go for water splitting: H_2O or OH^-? *Nanoscale* **2018**, 10, 15624-15631.
(23) Woo, T. K.; Margl, P. M.; Blöchl, P. E.; Ziegler, T. A Combined car−parrinello QM/MM implementation for ab Initio molecular dynamics simulations of extended systems: application to transition metal catalysis. . *J. Phys. Chem. B* **1997,** *101*, 7877-7880.
(24) Jarzynski, C. Nonequilibrium equality for free energy differences. *Phys. Rev. Lett.* **1997,** *78*, 2690-2693.
(25) Oberhofer, H.; Dellago, C. G., P. L. , Biased sampling of nonequilibrium trajectories: can fast switching simulations outperform conventional free energy calculation methods? . *J. Phys. Chem. B* **2005,** *109*, 6902-6915.
(26) Zhao, X.; Liu, Y., Unveiling the active structure of single nickel atom catalysis: critical roles of charge capacity and hydrogen bonding. *J. Am. Chem. Soc.* **2020,** *142* (12), 5773-5777.

(27) Ryckaert, J.-P.; Ciccotti, G.; Berendsen, H. Numerical integration of the cartesianequations of motion of a system with constraints: molecular dynamics of n-alkanes. *J. Comput. Phys.* **1997**, 23, 327-341.

(28) Nong, H. N.; Reier, T.; Oh, H. S.; Gliech, M.; Paciok, P.; Vu, T. H. T.; Teschner, D.; Heggen, M.; Petkov, V.; Schlögl, R.; Jones, T.; Strasser, P. A unique oxygen ligand environment facilitates water oxidation in hole-doped $IrNiO_x$ core–shell electrocatalysts. *Nat. Catal.* **2018**, 1, 841-851.

(29) Cheng, J.; Yang, J.; Kitano, S.; Juhasz, G.; Higashi, M.; Sadakiyo, M.; Kato, K.; Yoshioka, S.; Sugiyama, T.; Yamauchi, M.; Nakashima, N. Impact of Ir-valence control and surface nanostructure on oxygen evolution reaction over a highly efficient Ir–TiO_2 nanorod catalyst. *ACS Catal.* **2019**, 9, 6974-6986.

(30) Nellist, M. R.; Laskowski, F. A.; Lin, F.; Mills, T. J.; Boettcher, S. W. Semiconductor–electrocatalyst interfaces: theory, experiment, and applications in photoelectrochemical water splitting. *ACC Chem. Res.* **2016**, 49, 733-740.

(31) Mills, T. J.; Lin, F.; Boettcher, S. W. Theory and simulations of electrocatalyst-coated semiconductor electrodes for solar water splitting. *Phys. Rev. Lett.* **2014**, 112, 148304.

(32) Kawase, Y.; Obata, K.; Shioiri, Y.; Higashi, T.; Takanabe, K. Operando measurement of electrocatalyst potential on particulate photocatalysts for overall water splitting. *J. Mater. Chem. A* **2024**, 19352-19361.

(33) Shioiri, Y.; Obata, K.; Kawase, Y.; Higashi, T.; Katayama, M.; Schleuning, M., Krol, R.; Friedrich, D.; Abdi, F. F.; Takanabe, K. Estimating the quasi-Fermi level of holes at the surface of semiconductor photoanodes using outer-sphere redox couples. *Nat. Commun.* **2025**, 16, 3688.

(34) Zare Pour, M. A.; Qaisrani, M. N.; Höhn, C.; Wolf, J. L.; Mogharehabed, N.; Velazquez Rojas, J.; Jaegermann, W.; Runge, E.; van de Krol, R.; Hannappel, T.; Dreßler, C.; Paszuk, A. Composition and Resulting Band Alignment at the TiO_2/InP Heterointerface: A Fundamental Study Combining Photoemission Spectroscopy and Theory. *Adv. Funct. Mater.* **2026**, 36, 2506105.

(35) Wang, P.; Benitez, G.; Houle, F. A. Influence of hole transport and thermal reactions in photo-driven water oxidation kinetics on crystalline TiO_2. *ACS catal.* **2025**, 15, 7653-7665.

(36) Ooka, H.; Wintzer, M. E.; Nakamura, R. Non-zero binding enhances kinetics of catalysis: Machine learning analysis on the experimental hydrogen binding energy of platinum. *ACS Catal.* **2021**, 11, 6298–6303